

Direct Fidelity Estimation of Quantum States using Machine Learning

Xiaoqian Zhang,^{1,*} Maolin Luo,^{1,*} Zhaodi Wen,² Qin Feng,¹ Shengshi Pang,¹ Weiqi Luo,² and Xiaoqi Zhou^{1,†}

¹School of Physics and State Key Laboratory of Optoelectronic Materials and Technologies, Sun Yat-sen University, Guangzhou 510000, China

²College of Information Science and Technology, College of Cyber Security, Jinan University, Guangzhou 510632, China

(Dated: December 23, 2024)

In almost all quantum applications, one of the key steps is to verify that the fidelity of the prepared quantum state meets the expectations. In this paper, we propose a new approach to solve this problem using machine learning techniques. Compared to other fidelity estimation methods, our method is applicable to arbitrary quantum states, the number of required measurement settings is small, and this number does not increase with the size of the system. For example, for a general five-qubit quantum state, only four measurement settings are required to predict its fidelity with $\pm 1\%$ precision in a non-adversarial scenario. This machine learning-based approach for estimating quantum state fidelity has the potential to be widely used in the field of quantum information.

In the field of quantum information, almost all quantum applications require the generation and manipulation of quantum states. However, due to the imperfections of equipment and operation, the prepared quantum state is always different from the ideal state. Therefore, it is a key step to evaluate the deviation of the prepared state from the ideal one in the quantum applications. Quantum state tomography (QST) [1, 2, 4–17] is the standard method for reconstructing a quantum state to obtain its density matrix, which can be used to calculate the fidelity of the quantum state with respect to the ideal one. In recent years, researchers have proposed compressed sensing methods [5–10] to improve the efficiency of QST for the pure quantum states. Despite the fact that compressed sensing greatly reduces the measurement resources, the measurement settings for QST still grow exponentially with the size of the system.

However, to evaluate the fidelity of a quantum state, full reconstruction of its density matrix is not needed. Recently, schemes [18–37] for directly estimating the fidelity of quantum states, including the quantum state verification (QSV) method [26–37] and the direct fidelity estimation (DFE) method [20], have been proposed. The QSV method can determine whether a quantum state is the target state with few measurement resources, but this method is only applicable to special quantum states, such as the stabilizer states or the W states, and is not applicable to general quantum states. Compared with the QSV method, the DFE method [20] is applicable to general quantum pure states but requires more measurement settings. In most practical experiments, the number of measurement settings has a significant impact on the total measurement time (changing measurement setting is time-consuming). Both the QSV and the DFE methods assume that the measured quantum state may be prepared or manipulated by an adversary, which is valid for the case of quantum networks. For most local experiments in which the quantum devices are trusted, the imperfections of the quantum state are caused by noise and device defects, not by the adversary. As a result, our aim is to devise a direct fidelity estimation protocol for this scenario, further reducing the number of measurement

settings required.

In this work, we use machine learning methods [1, 38–45, 47] to tackle this problem. So far, machine learning methods have been used for classification problems [38–43] in the field of quantum information to detect the non-locality [38], steerability [40], entanglement [39] and coherence [47] of quantum states. In these previous works, the classification of quantum states can be performed with high accuracy using fewer measurement settings by using artificial neural networks (ANNs) to learn the potential information between the internal structures of the quantum state space. In this work, we transform the quantum state fidelity estimation problem into a classification problem, by dividing the quantum state space into different subspaces according to the value of fidelity, and then using a neural network to predict which subspace the quantum state is in to obtain an estimate of the quantum state fidelity. Compared with previous methods for direct estimation of fidelity, this method not only works for arbitrary quantum states, but also greatly reduces the number of measurement settings required.

Representing fidelity using Pauli observables.—The fidelity [48] of an arbitrary quantum state ρ with respect to the desired pure state ρ_0 can be written as

$$F(\rho_0, \rho) = \text{tr} \sqrt{\rho^{1/2} \rho_0 \rho^{1/2}} = \sqrt{\text{tr}(\rho \rho_0)}, \quad (1)$$

where

$$\rho_0 = \frac{1}{2^n} \sum_{j=0}^{4^n-1} a_j W_j, \quad \rho = \frac{1}{2^n} \sum_{j=0}^{4^n-1} \beta_j W_j. \quad (2)$$

Here W_j represents Pauli operators which are n -fold tensor products of $I, \sigma_x, \sigma_y, \sigma_z$. The fidelity in Eq.(1) can be expanded in terms of the Pauli operators' expectation values a_j and β_j ,

$$F(\rho_0, \rho) = \sqrt{\frac{1}{2^n} \sum_{j=0}^{4^n-1} \beta_j a_j}. \quad (3)$$

The artificial neural networks.—For an n -qubit quantum state, there exist 3^n Pauli operators consisting of a tensor product of σ_x, σ_y and σ_z , from which k Pauli operators are selected for measurement. Here we have chosen the k Pauli operators with the largest absolute value of the expectation value of the

* These authors contributed equally

† zhouxq8@mail.sysu.edu.cn

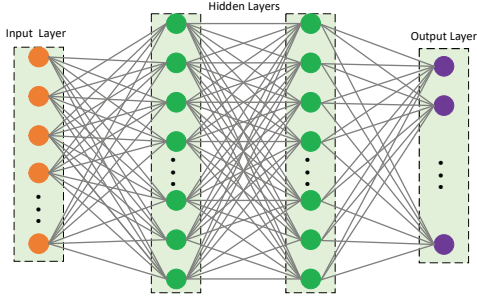


FIG. 1. (Color online) The artificial neural network for quantum state fidelity evaluation. The input layer neurons are loaded with the measurements of the Pauli operators, the output layer neurons correspond to different fidelity intervals, and the input and output layers are fully connected by several hidden layers. After hundreds of training sessions, a neural network model that can evaluate the fidelity of quantum states is obtained.

desired quantum state. For each of these k Pauli operators, there are 2^n possible outcomes and the probability of each outcome occurring will be used as an input. Thus the input layer has a total of $k \times 2^n$ neurons. The input layer neurons are fully connected to the hidden layer, i.e., each neuron of the input layer is connected to each neuron of the hidden layer. The hidden layer is also fully connected to the output layer. The output layer has a total of 122 neurons corresponding to different fidelity intervals of the quantum states. We generated various quantum states of different fidelity using the program we designed (see Supplementary Information) and calculated the $k \times 2^n$ probability values corresponding to each quantum state and its fidelity label which ranges from 1 to 122. For each fidelity interval, we generated 20,000 quantum states, 16,000 of which were used for neural network training and 4,000 for neural network validation. After several hundred rounds of training, the prediction accuracy of the neural network saturates, resulting in a neural network model that can predict the fidelity of the quantum states with high confidence (See Supplementary Information).

Taking a general five-qubit quantum state $|\psi_0\rangle$ as an example [49], by setting $k = 2, 3, 4$, and 5 and four different neural network models are generated respectively using the methods described above to predict the fidelity of the input quantum state with respect to $|\psi_0\rangle$. When predicting fidelity with a neural network model, the accuracy of the prediction is inversely related to the confidence level, and here we set the confidence level fixed at 95%. Figure 2 shows that the higher the number of Pauli operators used, the higher the prediction accuracy of the neural network model is. For the same neural network model, the higher the value of the predicted fidelity, the higher the accuracy of that prediction is.

Now we look at how to use a neural network model for a specific problem—to determine whether the fidelity of the input quantum states $|\psi_1\rangle$ and $|\psi_2\rangle$ (See Supplementary Information) with respect to $|\psi_0\rangle$ exceeds 96%. For $|\psi_1\rangle$, we choose the top three Pauli operators in the absolute value of the expectation value for measurement, and input the measurement results into the neural network model with $k = 3$, and obtain

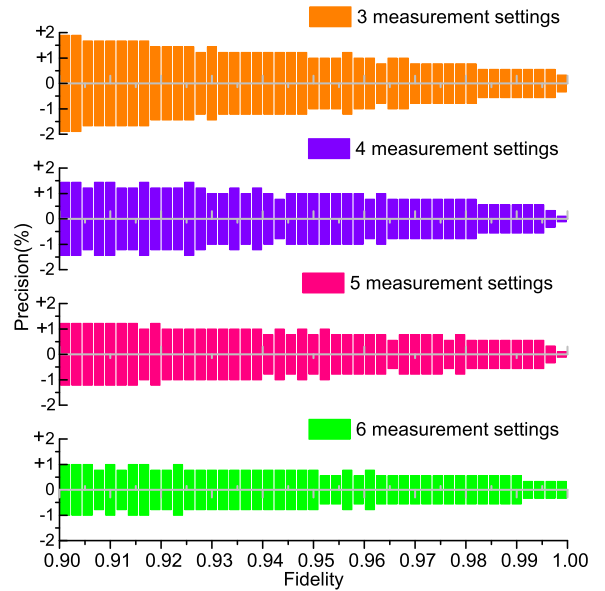


FIG. 2. (Color Online) A plot of the prediction accuracy of the neural network versus the quantum state fidelity when measurements are made using three, four, five, and six Pauli operator measurement settings. The higher the number of Pauli operator measurement settings used, the higher the prediction accuracy is. The higher the fidelity of the predicted quantum states is, the higher the accuracy is.

a fidelity prediction of $(97.67 \pm 0.78)\%$, which indicates the fidelity of $|\psi_1\rangle$ exceeds 96%. For $|\psi_2\rangle$, repeating the above operations, the fidelity result obtained is $(95.45 \pm 1.22)\%$, which cannot indicate whether the fidelity of $|\psi_1\rangle$ exceeds 96% for now. Then the Pauli operator with the fourth largest absolute value of expectation value is measured, and the measurement result was input into the $k = 4$ neural network model together with the measurement results of the first three Pauli operators, and the fidelity prediction result obtained is $(94.78 \pm 0.78)\%$, indicating that the fidelity of $|\psi_2\rangle$ does not exceed 96%.

Figure 3 illustrates the cases of n -qubit quantum states (n ranges from 2 to 6), indicating that the number of Pauli operators that need to be measured does not increase as the number of qubits of the quantum state increases. For example, for a general six-qubit quantum state, only three Pauli operators are needed for measurement to make predictions about the fidelity. This phenomenon seems a bit counterintuitive, and it can be understood as follows: when the fidelity is $1, \beta_j$, the expectation value of Pauli operators for the input quantum state, will be equal to a_j , the expectation value of Pauli operators for the desired quantum state. When the fidelity is less than 1, β_j deviates with respect to a_j , and the smaller the fidelity, the larger this deviation will be. Since we consider the non-adversarial scenario, the deviation of β_j with respect to a_j will not be particularly preferred to specific Pauli operators. A fraction of β_j , which can be derived from the measurement results of the k Pauli bases, is equivalent to a sampling of the

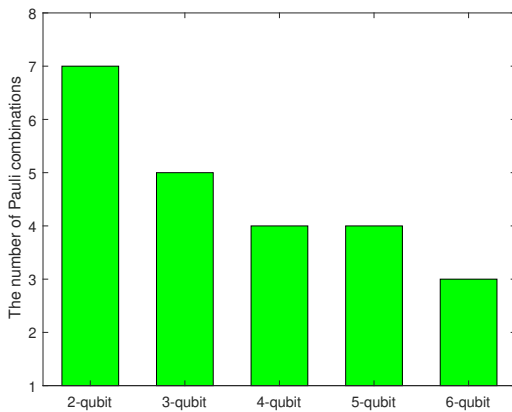


FIG. 3. (Color Online) For general quantum states (fidelity between 0.95 and 1) with two, three, four, five, and six qubits, the number of Pauli operator measurement settings required to predict fidelity with $\pm 1\%$ accuracy using neural network models, are 7, 5, 4, 4, and 3, respectively.

entire set of β_j . Therefore, by comparing the deviation of this fraction of β_j with the corresponding fraction of a_j , the deviation of the entire set of β_j with respect to the entire set of a_j can be estimated, and thus the fidelity of the input state with

respect to the ideal state can be predicted.

To summarize, we present in this paper a method for predicting the fidelity of quantum states using neural network models. Compared with previous methods for quantum state fidelity estimation, our method uses fewer measurement settings and works for arbitrary quantum states. Here our method is applicable to non-adversarial scenarios. It has the potential to be used in a wide variety of local quantum information applications, such as quantum computation, quantum simulation, and quantum metrology. A future research direction is to design machine-learning-based quantum state fidelity estimation schemes in adversarial scenarios.

This work was supported by the National Key Research and Development Program (2017YFA0305200 and 2016YFA0301700), the Key Research and Development Program of Guangdong Province of China (2018B030329001 and 2018B030325001), the National Natural Science Foundation of China (Grant No. 61974168). X. Zhou acknowledges support from the National Young 1000 Talents Plan. W. Luo acknowledges support from the National Natural Science Foundation of China (Grant No. 61877029). X. Zhang acknowledges support from the National Natural Science Foundation of China (Grant No. 62005321). S. Pang acknowledges support from the National Natural Science Foundation of China (Grant No. 12075323).

[1] A. Chantasri, S.-S. Pang, T. Chalermpusitarak, A. N. Jordan, Quantum state tomography with time-continuous measurements: reconstruction with resource limitations, *Quantum Stud.: Math. Found.* 7 (2020) 23–47.

[2] G. Toth, W. Wieczorek, D. Gross, R. Krischek, C. Schwemmer, H. Weinfurter, Permutationally invariant quantum tomography, *Phys. Rev. Lett.* 105 (2010) 250403.

[3] M. Cramer, M. B. Plenio, S. T. Flammia, R. Somma, D. Gross, S. D. Bartlett, O. Landon-Cardinal, D. Poulin, Y. Liu, Efficient quantum state tomography, *Nature Communications* 1 (2010) 149.

[4] J. Renes, R. Blume-Kohout, A. Scott, C. Caves, Symmetric informationally complete quantum measurements, *J. Math. Phys.* 45(6) (2004) 2171–2180.

[5] D. Gross, Y. Liu, S. T. Flammia, S. Becker, J. Eisert, Quantum state tomography via compressed sensing, *Phys. Rev. Lett.* 105 (2010) 150401.

[6] S. T. Flammia, D. Gross, Y. Liu, J. Eisert, Quantum tomography via compressed sensing: error bounds, sample complexity and efficient estimators, *New J. Phys.* 14 (2012) 095022.

[7] A. Smith, C. A. Riofrío, B. E. Anderson, H. Sosa-Martinez, I. H. Deutsch, P. S. Jessen, Quantum state tomography by continuous measurement and compressed sensing, *Phys. Rev. A* 87 (2013) 030102(R).

[8] A. Kalev, R. L. Kosut, I. H. Deutsch, Quantum tomography protocols with positivity are compressed sensing protocols, *npj Quantum Information* 1 (2015) 15018.

[9] C. Riofrío, D. Gross, S. Flammia, T. Monz, D. Nigg, R. Blatt, J. Eisert, Experimental quantum compressed sensing for a seven-qubit system, *Nat. Commun.* 8 (2017) 15305.

[10] A. Kyrillidis, A. Kalev, D. Park, S. Bhojanapalli, C. Caramanis, S. Sanghavi, Provable compressed sensing quantum state tomography via non-convex methods, *npj Quantum Information* 4 (2018) 36.

[11] J. Shang, Z. Zhang, H. K. Ng, Superfast maximum-likelihood reconstruction for quantum tomography, *Phys. Rev. A* 95 (2017) 062336.

[12] G. Silva, S. Glancy, H. Vasconcelos, Investigating bias in maximum-likelihood quantum-state tomography, *Phys. Rev. A* 95 (2017) 022107.

[13] C. Oh, Y. Teo, H. Jeong, Efficient bayesian credible region certification for quantum-state tomography, *Phys. Rev. A* 100 (2019) 012345.

[14] V. Siddhu, Maximum a posteriori probability estimates for quantum tomography, *Phys. Rev. A* 99 (2019) 012342.

[15] X. Ma, H. Z. T. Jackson, J.-X. Chen, D.-W. Lu, M. D. Mazurek, K. A. G. Fisher, X.-H. Peng, D. Kribs, K. J. Resch, Z.-F. Ji, B. Zeng, R. Laflamme, Pure-state tomography with the expectation value of pauli operators, *Phys. Rev. A* 93 (2016) 032140.

[16] D. Martnez, M. SolI-Prosser, G. Cañas, O. Jiménez, A. Delgado, G. Lima, Experimental quantum tomography assisted by multiply symmetric states in higher dimensions, *Phys. Rev. A* 99 (2019) 012336.

[17] H. Sosa-Martinez, N. Lysne, C. Baldwin, A. Kalev, I. Deutsch, P. Jessen, Experimental study of optimal measurements for quantum state tomography, *Phys. Rev. A* 119 (2017) 150401.

[18] C. Y. L. O. Gühne, W. B. Gao, J. W. Pan, Toolbox for entanglement detection and fidelity estimation, *Phys. Rev. A* 76 (2007) 030305(R).

[19] Y. Tokunaga, T. Yamamoto, M. Koashi, N. Imoto, Fidelity

estimation and entanglement verification for experimentally produced four-qubit cluster states, *Phys. Rev. A* 74 (2006) 020301(R).

[20] S. T. Flammia, Y. K. Liu, Direct fidelity estimation from few pauli measurements, *Phys. Rev. Lett.* 106 (2011) 230501.

[21] da S. Marcus P., L. C. Olivier and P. David, Practical Characterization of Quantum Devices without Tomography, *Phys. Rev. Lett.* 107 (2011) 210404.

[22] H. J. Zhu, M. Hayashi, Optimal verification and fidelity estimation of maximally entangled states, *Phys. Rev. A* 99 (2019) 052346.

[23] M. Cerezo, A. Poremba, L. Cincio, P. J. Coles, Variational quantum fidelity estimation, *Quantum* 4(248) (2020) 1-16.

[24] D. S. Rolando, J. Chiaverini, D. J. Berkeland, Lower bounds for the fidelity of entangled-state preparation, *Phys. Rev. A* 74 (2006) 052302.

[25] J. Wang, Z. Han, S. Wang, Z. Li, L. Mu, H. Fan, L. Wang, Scalable quantum tomography with fidelity estimation, *Phys. Rev. A* 101 (2020) 032321.

[26] D. Mahler, L. A. Rozema, A. Darabi, C. Ferrie, R. Blume-Kohouz, A. Steinberg, Adaptive quantum state tomography improves accuracy quadratically, *Phys. Rev. Lett.* 111 (2013) 183601.

[27] Z.-H. Li, Y.-G. Han, H.-J. Zhu, Efficient verification of bipartite pure states, *Phys. Rev. A* 100 (2019) 032316.

[28] X.-D. Yu, J.-W. Shang, O. Gühne, Optimal verification of general bipartite pure states, *npj Quantum Information* 5 (2019) 112.

[29] H.-J. Zhu, M. Hayashi, Efficient verification of pure quantum states in the adversarial scenario, *Phys. Rev. Lett.* 123 (2019) 260504.

[30] Y.-C. Liu, X.-D. Yu, J.-W. Shang, H.-J. Zhu, X.-D. Zhang, Efficient verification of dicke states, *Phys. Rev. APPL.* 12 (2019) 044020.

[31] H.-J. Zhu, M. Hayashi, Efficient verification of hypergraph states, *Phys. Rev. APPL.* 12 (2019) 054047.

[32] K. Wang, M. Hayashi, Optimal verification of two-qubit pure states, *Phys. Rev. A* 100 (2019) 032315.

[33] H.-J. Zhu, M. Hayashi, General framework for verifying pure quantum states in the adversarial scenario, *Phys. Rev. A* 100 (2019) 062335.

[34] Y.-G. H. Z.-H. Li, H.-J. Zhu, Optimal verification of greenberger-horne-zeilinger states, *Phys. Rev. APPL.* 13 (2020) 054002.

[35] S. Pallister, N. Linden, A. Montanaro, Optimal verification of entangled states with local measurements, *Phys. Rev. Lett.* 120 (2018) 170502.

[36] W.-H. Zhang, C. Zhang, Z. Chen, X.-X. Peng, X.-Y. Xu, P. Yin, S. Yu, X.-J. Ye, Y.-J. Han, J.-S. Xu, G. Chen, C.-F. Li, G.-C. Guo, Experimental optimal verification of entangled states using local measurements, *Phys. Rev. Lett.* 125.

[37] X. H. Jiang, K. Wang, K. Y. Qian, Z. Z. Chen, Z. Y. Chen, L. L. Lu, L. J. Xia, F. M. Song, S. N. Zhu and X. S. Ma, Towards the standardization of quantum state verification using optimal strategies, *npj Quantum Information* 6(2020) 90.

[38] M. Yang, C. Ren, Y. Ma, Y. Xiao, X. Ye, Experimental simultaneous learning of multiple nonclassical correlations, *Phys. Rev. Lett.* 123 (2019) 190401.

[39] Y.-C. Ma, M.-H. Yung, Transforming bell's inequalities into state classifiers with machine learning, *npj Quantum Information* 4 (2018) 34.

[40] S.-R. Lu, S.-L. Huang, K.-R. Li, J. Li, J.-X. Chen, D.-W. Lu, Z.-F. Ji, Y. Shen, D.-L. Zhou, B. Zeng, Separability-entanglement classifier via machine learning, *Phys. Rev. A* 98 (2018) 012315.

[41] J. Gao, L.-F. Qiao, Z.-Q. Jiao, Y.-C. Ma, C.-Q. Hu, R.-J. Ren, A.-L. Yang, H. Tang, M.-H. Yung, X.-M. Jin, Experimental machine learning of quantum states, *Phys. Rev. Lett.* 120 (2018) 240501.

[42] D.-L. Deng, Machine learning detection of bell nonlocality in quantum many-body systems, *Phys. Rev. Lett.* 120 (2018) 240402.

[43] C.-L. Ren, C.-B. Chen, Steerability detection of an arbitrary two-qubit state via machine learning, *Phys. Rev. A* 100 (2019) 022314.

[44] T. Xin, S.-R. Lu, N.-P. Cao, G. Anikeeva, D.-W. Lu, J. Li, G.-L. Long, B. Zeng, Local-measurement-based quantum state tomography via neural networks, *npj Quantum Information* 5 (2019) 109.

[45] A. Ling, K.-P. Soh, A. Lamas-Linares, C. Kurtsiefer, Experimental polarization state tomography using optimal polarimeters, *Phys. Rev. A* 74 (2006) 022309.

[46] J. A. Miszczak, Generating and using truly random quantum states in mathematica, *Computer Physics Communications* 183 (2012) 118–124.

[47] Q. M. Ding, X. X. Fang, X. Yuan, T. Zhang, H. Lu, Efficient estimation of multipartite quantum coherence, *arXiv:2010.02612v2 [quant-ph]* 15 Oct 2020.

[48] F. Tacchino, C. Macchiavello, D. Gerace, D. Bajoni, Measurement of qubits, *Phys. Rev. A* 64 (2001) 052312.

[49] The five-qubit state can be represented by the following vector $[0.1592 + 0.0000i; 0.0474 - 0.1834i; -0.0431 - 0.1664i; -0.3363 - 0.0787i; -0.0380 - 0.1645i; 0.0378 - 0.0606i; -0.0846 + 0.2026i; 0.1586 + 0.2416i; 0.1116 - 0.0157i; 0.1064 + 0.0906i; 0.0608 - 0.1556i; 0.0302 - 0.0418i; -0.0254 - 0.0624i; -0.0319 - 0.2507i; 0.0381 - 0.1123i; -0.1093 - 0.1652i; -0.0873 - 0.1461i; 0.1807 - 0.1654i; 0.2658 + 0.0427i; -0.2010 - 0.0322i; 0.0356 - 0.0686i; 0.1222 + 0.0009i; 0.0944 + 0.1331i; 0.0080 + 0.0417i; -0.0748 - 0.0483i; 0.0762 + 0.0756i; 0.1541 - 0.0227i; -0.1414 + 0.1879i; -0.1427 + 0.0462i; -0.1530 - 0.0816i; 0.0003 - 0.1342i; -0.1308 - 0.0317i].$

SUPPLEMENTARY MATERIALS

In this supplementary material, we discuss more results. Sec.(I) describes the basic structure of artificial neural networks (ANNs) and our artificial neural network. Sec.(II) gives the method to generate quantum states with specified fidelity. It also analyzes the uniformity of pure state fidelity, mixed state fidelity The purity distribution of mixed states, the generality of our method, and Poisson noise are also presented here. The method for selecting the Pauli operators is given in Sec.(III). Sec.(IV) compares the accuracy of the neural network at two different inputs, i.e., the probability of each outcome and the expectation values of the Pauli operators. Sec.(V) analyzes the accuracy of the quantum state fidelity estimation. Sec.(VI) gives the verification accuracy of the neural network. Sec.(VII) presents a practical application of our neural network.

I. THE STRUCTURE OF ANNS AND OUR ANN

The basic structure of ANNs

ANNS consists of an input layer, hidden layers and an output layer (See FIG.1). The input layer consists of $k \times 2^n$ neurons corresponding to the probability of each outcome, in which n represents the number of qubits and k represents the number of Pauli combinations. We set the inputs \mathbf{x}_0 and the intermediate vector \mathbf{x}_1 in the hidden layer generated by the non-linear relation

$$\mathbf{x}_1 = \sigma_{RL}(\mathbf{W}_1 \mathbf{x}_0 + \omega_1), \quad (4)$$

where σ_{RL} is the ReLU function for each neuron in the hidden layer, defined as $\sigma_{RL}(z_i) = \max(z_i, 0)$ ($i = 1, 2, 3, \dots$). The matrix \mathbf{W}_1 is the initialized weight and the vector ω_1 is the bias between the input layer and the hidden layer. The optimal output vector denoted as \mathbf{x}_2 is generated using the function

$$\mathbf{x}_2 = \sigma_s(\mathbf{W}_2 \mathbf{x}_1 + \omega_2), \quad (5)$$

where σ_s is the Softmax function defined by $\sigma(z_i) = \frac{e^{z_i}}{\sum_{k=1}^{122} e^{z_k}}$ ($i = 1, \dots, 122$). The matrix \mathbf{W}_2 is the initialized weight between the hidden layer and the output layer, while the vector ω_2 is the bias. The loss function is categorical cross-entropy and is written as $-\frac{1}{n} [y_s \log a_s + (1 - y_s) \log(1 - a_s)]$. The subscript s denotes the sequence number of the training sample, and the notation y represents the labels defined by the criterion, a means the output labels of the ANN and n is the training set number, respectively. During the machine learning process, $\mathbf{W}_1, \omega_1, \mathbf{W}_2, \omega_2$ are continuously optimized until the confidence level reaches saturation, and then the training is stopped.

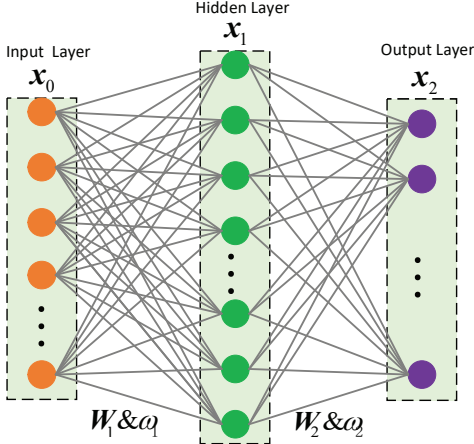


FIG. 4. (Color online) Artificial neural networks with hidden layers. The objective of machine learning is to optimize $\sigma_s(\mathbf{W}_2 \sigma_{RL}(\mathbf{W}_1 \mathbf{x}_0 + \omega_1) + \omega_2)$, where $\sigma_{RL}(z_i) = \frac{e^{z_i}}{\sum_{k=1}^{122} e^{z_k}}$ ($i = 1, 2, \dots, K$) is softmax function. The input data $\mathbf{x}_0 = \{\mathbf{a}_1, \mathbf{a}_2, \dots, \mathbf{a}_k\}$ are the measurements of Pauli operators. Matrix \mathbf{W}_1 and the vector ω_1 are initialized uniformly and optimized during the learning process. The number of neurons in the hidden layer can be varied for optimal performance. The output data \mathbf{x}_2 are the predicted fidelity.

The ANN for fidelity estimation

We use four 2080Ti GPUs. We choose the optimizer that has the best performance in our task among almost all the built-in optimizers in TensorFlow: NadamOptimizer (adaptive moment estimation). This neural network contains 122

labels, using 1,952,000 data for training and 488,000 data for validation, i.e. each label contains 16,000 training data and 4,000 validation data. By tuning the batch size of inputs, the number of neurons, and the number of training rounds, the performance of the neural network is continuously optimized. Eventually, the parameters required for training this neural network from two-qubit to seven-qubit quantum states are shown in Table S1. Hid-neu represents the number of the hidden neurons.

Table S1. Parameters of our ANN

two-qubit states				three-qubit states			
state	epoch	Batch size	Hid-neu	state	epoch	Batch size	Hid-neu
Bell	200	2048	1000	GHZ	400	4096	1000
W			2000	W			2000
$ \varphi_2\rangle$			3000	$ \varphi_3\rangle$			3000
four-qubit states				five-qubit states			
state	epoch	Batch size	Hid-neu	state	epoch	Batch size	Hid-neu
Cluster				Cluster			
W				C-ring			500-500
GHZ	400	8192	2000	Dicke			1000-1000
Dicke			3000	GHZ			1500-1500
$ \varphi_4\rangle$			5000	W			
six-qubit states				seven-qubit states			
state	epoch	Batch size	Hid-neu	state	epoch	Batch size	Hid-neu
C_{23}				C_{34}			
Dicke	500	16384	500-500				300-600-300
GHZ			1000-1000				500-1000-500
W			1500-1500				700-1400-700
$ \varphi_6\rangle$							

Next, we show the specific forms of the special number states that appear in Table S1 (See FIG.2). Moreover, $|\varphi_2\rangle, |\varphi_3\rangle, |\varphi_4\rangle, |\varphi_5\rangle, |\varphi_6\rangle$ are general quantum states [5]. The two-qubit Bell state and the W state are

$$|\phi^+\rangle_{Bell} = \frac{1}{\sqrt{2}}(|00\rangle + |11\rangle), \quad (6)$$

$$|W\rangle = \frac{1}{\sqrt{3}}(|00\rangle + |01\rangle + |10\rangle).$$

The three-qubit GHZ state and the W state are

$$|GHZ\rangle = \frac{1}{\sqrt{2}}(|000\rangle + |111\rangle), \quad (7)$$

$$|W\rangle = \frac{1}{\sqrt{3}}(|001\rangle + |010\rangle + |100\rangle).$$

The four-qubit Cluster state, the Dicke state, the GHZ state and the W state are

$$|Cluster_4\rangle = \frac{1}{2}(|0000\rangle + |0011\rangle + |1100\rangle - |1111\rangle),$$

$$|Dicke_4^2\rangle = \frac{1}{\sqrt{6}}(|0011\rangle + |0110\rangle + |0101\rangle + |1010\rangle + |1001\rangle + |1100\rangle),$$

$$|GHZ\rangle = \frac{1}{\sqrt{2}}(|0000\rangle + |1111\rangle),$$

$$|W\rangle = \frac{1}{2}(|0001\rangle + |0010\rangle + |0100\rangle + |1000\rangle).$$
(8)

The five-qubit Cluster state, the C-ring state, the Dicke state, the GHZ state and the W state are

$$\begin{aligned}
 |\text{Cluster}_5\rangle &= \frac{1}{2}(|+0+0+\rangle + |+0-1-\rangle + |-1-0+\rangle + |-1-1-\rangle), \\
 |\text{C-rings}\rangle &= \frac{1}{2\sqrt{2}}(|+0+00\rangle + |-0+01\rangle \\
 &\quad + |-0-10\rangle - |-0-11\rangle + |-1-00\rangle \\
 &\quad + |-1-01\rangle + |-1+10\rangle - |+1+11\rangle), \\
 |\text{Dicke}_5^2\rangle &= \frac{1}{\sqrt{10}}(|11000\rangle + |10100\rangle + |01100\rangle \\
 &\quad + |01010\rangle + |00110\rangle + |00101\rangle + |00011\rangle \\
 &\quad + |10010\rangle + |10001\rangle + |01001\rangle), \\
 |\text{GHZ}\rangle &= \frac{1}{\sqrt{2}}(|00000\rangle + |11111\rangle), \\
 |\text{W}\rangle &= \frac{1}{\sqrt{5}}(|10000\rangle + |01000\rangle + |00100\rangle + |00010\rangle + |00001\rangle).
 \end{aligned}$$

The six-qubit Cluster state, the Dicke state, the GHZ state and the W state are

$$\begin{aligned}
 |\text{C23}\rangle &= \frac{1}{2}(|+0+0++0+\rangle + |+0+0-1-\rangle + |-1-0+0+\rangle - |-1-1-1-\rangle), \\
 |\text{Dicke}_6^2\rangle &= \frac{1}{\sqrt{15}}(|000011\rangle + |000101\rangle + |001010\rangle \\
 &\quad + |001100\rangle + |110000\rangle + |010100\rangle + |101000\rangle \\
 &\quad + |001001\rangle + |010001\rangle + |100001\rangle + |100010\rangle \\
 &\quad + |100100\rangle + |000110\rangle + |011000\rangle + |010010\rangle), \\
 |\text{GHZ}\rangle &= \frac{1}{\sqrt{2}}(|000000\rangle + |111111\rangle), \\
 |\text{W}\rangle &= \frac{1}{\sqrt{6}}(|000001\rangle + |000010\rangle + |000100\rangle + |010000\rangle + |100000\rangle)
 \end{aligned}$$

The seven-qubit Cluster state is

$$\begin{aligned}
 |\text{C34}\rangle &= \frac{1}{2\sqrt{2}}(|+00+0+0+\rangle + |+00+0-1-\rangle \\
 &\quad + |-01-0+\rangle + |-01-1-\rangle \\
 &\quad + |-10+0+\rangle - |-10+1-\rangle \\
 &\quad - |-11+0+\rangle + |-11-1-\rangle).
 \end{aligned} \quad (11)$$

II. GENERATION AND ANALYSIS OF QUANTUM STATES

A. Generation of quantum pure states with specified fidelity
 Preparing quantum states has an important role in realizing quantum information and quantum computing, but often the imperfection of devices and the influence of noise result in obtaining quantum states that are all mixed states. Here, we use neural network techniques to evaluate whether the fidelity between this quantum state and the ideal state satisfies the requirements. Our neural network inputs are derived from mixed states with specified fidelity. We first introduce the method for generating a pure state.

Step 1. Generating an arbitrary pure state

In Mathematics, we create a pure state of arbitrary dimension with the help of the function *RandomKet(D)* [1]. Specifically, The *RandomKet(D)* function calls *RandomSimplex(D)* and *Randomreal(D)* to generate a D-dimensional arbitrary pure state. The Mathematica code of generating an arbitrary pure state is shown below.

```

RandomSimplex [ d_]:= Block [ { r , r1 , r2 } ,
r=Sort [ Table [ RandomReal [ { 0 , 1 } ] , { i , 1 , d-1 } ] ];
r2=Append [ r , 1 ];
r1=Prepend [ r , 0 ]; r1-r2
];

RandomKet[ n_]:= Block [ { p , ph } ,
p= Sqrt [ RandomSimplex [ n ] ];
p0=Exp [ I RandomReal [ { 0 , 2\ [ Pi ] } , n-1 ] ];
ph=Prepend [ ph , 1 ];
p*ph
];

```

Step 2. Generation of a pure state with specified fidelity corresponding to the state $|0\rangle^{\otimes n}$
 An arbitrary pure state can be expanded as

$$|\varphi\rangle = \sum_{i=0}^{2^n-1} \alpha_i |i\rangle, \quad (12)$$

where $|i\rangle$ ($i = 0, 1, \dots, 2^n - 1$) is basis vector of calculations. For convenience, we rewrite Eq.(9) as follows.

$$(10)|\varphi\rangle = f|0\rangle^{\otimes n} + \sum_{i=1}^{2^n-1} \alpha_i |i\rangle = f|0\rangle + \sqrt{1-f^2}|\phi\rangle^{2^n-1}, \quad (13)$$

where $\alpha_0 = f$. The state $|\phi\rangle^{2^n-1}$ is a $(2^n - 1)$ dimensional arbitrary pure state. Therefore, the fidelity f between $|0\rangle^{\otimes n}$ and $|\varphi\rangle$ is given as

$$f = F(|0\rangle^{\otimes n}, |\varphi\rangle) = |\langle 0 |^{\otimes n} |\varphi \rangle| \quad (14)$$

Hence, we can generate an n -qubit pure state dataset with the target state $|0\rangle^{\otimes n}$ using Matlab.

Step 3. Generation of a pure state with a specified fidelity corresponding to an arbitrary pure state

For convenience, we set $|\mathbf{0}\rangle = |0\rangle^{\otimes n}$. Then we rewrite the Eq.(11) as follows.

$$f = F(|\mathbf{0}\rangle, \sigma) = \sqrt{\langle \mathbf{0} | \sigma | \mathbf{0} \rangle}, \quad (15)$$

where σ can be viewed as a state in the dataset S with a target state $|\mathbf{0}\rangle$. If we choose a new target pure state ρ , there is a unitary matrix transformation U from $|\mathbf{0}\rangle\langle \mathbf{0}|$ to ρ . This unitary U can be calculated by the code *Findunitary.m*. As soon as such unitary is found [2, 3], the relative state of σ is directly obtained as

$$\sigma' = U\sigma U^\dagger, \quad (16)$$

where the state σ' belongs to the database S' of the target state ρ . The fidelity f' between the target state ρ and the state σ' can be calculated, that is,

$$f' = F(\rho, \sigma') = \sqrt{\text{tr}(\rho, \sigma')} = \sqrt{\langle \mathbf{0} | U^\dagger \sigma' U | \mathbf{0} \rangle} = \sqrt{\langle \mathbf{0} | \sigma | \mathbf{0} \rangle} \in \mathcal{J}$$

Step 4. Projective measurements

Each measurement setting k is characterized by W_k , and each specific result $p(k_j)$ is associated with a projection operator

$$P_{k_j} = |v_{k_j}\rangle\langle v_{k_j}|, \quad j = 1, 2, \dots, 2^n, \quad (18)$$

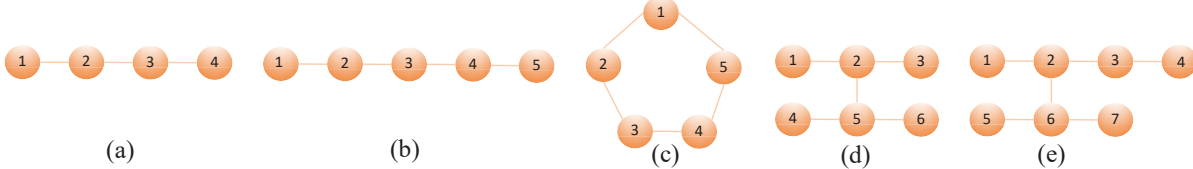


FIG. 5. The structure of Cluster states. (a) The four-qubit line Cluster state $|\text{Cluster}_4\rangle$. (b) The five-qubit line Cluster state $|\text{Cluster}_5\rangle$. (c) The five-qubit ring Cluster state $|\text{C-ring}\rangle$. (d) The six-qubit grid Cluster state $|\text{C23}\rangle$. (e) The seven-qubit Cluster state $|\text{C34}\rangle$.

where $|v_{k_j}\rangle$ is the j_{th} eigenvector of the W_k , $p(k_j)$ is equal to $\text{tr}(\rho P_{k_j})$.

B. Generation of quantum mixed states with specified fidelity

Here we give the method for generating mixed states with specified fidelity. In a Ginibre matrix G , each element is the standard complex normal distribution $CN(0, 1)$. The random density matrix of mixed states can be written as

$$\rho = \frac{GG^\dagger}{\text{tr}(GG^\dagger)}. \quad (19)$$

Inspired by the Ginibre matrix G , we propose a method to prepare specified fidelity states with the target state $|\mathbf{0}\rangle$, i.e., the density matrix of desired N-qubit mixed state is

$$\rho_n = \frac{\mathbb{G}_n \mathbb{G}_n^\dagger}{\text{tr}(\mathbb{G}_n \mathbb{G}_n^\dagger)}. \quad (20)$$

where the matrix \mathbb{G}_n can be expressed as

$$\mathbb{G}_n = \left(\sqrt{m_1} \left(\begin{array}{c} x_1 e^{-2\pi i * \text{rand}_{11}} \\ \sqrt{1 - x_1^2} e^{-2\pi i * \text{rand}_{12}} |\varphi_1\rangle \end{array} \right), \dots, \sqrt{m_n} \left(\begin{array}{c} x_n e^{-2\pi i * \text{rand}_{n1}} \\ \sqrt{1 - x_n^2} e^{-2\pi i * \text{rand}_{n2}} |\varphi_n\rangle \end{array} \right) \right) \quad (21)$$

The notations rand_{b1} and rand_{b2} ($b = 1, 2, \dots, n$) represent random numbers. The set $\{|\varphi_1\rangle, \dots, |\varphi_n\rangle\}$ is a collection of $2^n - 1$ dimensional pure states produced by the function *RandomKet*. $\{m_1, \dots, m_n\}$ is a set of real numbers of 2^N dimension normalized standard normal distribution. $\{x_1, \dots, x_n\}$ is a set of undefined real numbers that are closely related to the expected fidelity.

The steps for preparing the mixed state are similar to those for preparing the pure state. As can be seen from Eq.(18), the density matrix of a mixed state with specified fidelity needs to determine the values of $\{m_1, \dots, m_n\}$ and $\{x_1, \dots, x_n\}$, where the former is generated randomly using the Matlab code and

the latter is determined according to the corresponding constraints.

An example.—For a two-qubit state, suppose the desired fidelity is f_0 for the target state $|00\rangle$. The values $\{x_1, x_2, x_3, x_4\}$ in the matrix \mathbb{G}_n can be determined from Eqs. (19-22) using Matlab. The value range of x_1 can first be determined in Eq.(19) by the given fidelity f_0 . When we fix the x_1 randomly and uniformly, the value range of x_2 can also be determined in Eq.(20). Then we fix the x_2 randomly and uniformly, and the value range of x_3 can also be defined in Eq.(21). Once the value of x_3 is fixed randomly and uniformly, the value of x_4 is also fixed in Eq.(22). Therefore, we obtain the matrix \mathbb{G}_n .

$$x_1 \in (\min(\max(\frac{f_0^2 - \sum_{i=2}^4 m_i}{m_1}, 0), 1), \min(\max(\frac{f_0^2}{m_1}, 0), 1)), \quad (22)$$

$$x_2 \in (\min(\max(\frac{f_0^2 - m_1 x_1^2 \sum_{i=3}^4 m_i}{m_2}, 0), 1), \min(\max(\frac{f_0^2 - m_1 x_1^2}{m_2}, 0), 1)), \quad (23)$$

$$x_3 \in (\min(\max(\frac{f_0^2 - \sum_{i=1}^2 m_i x_i^2 - m_4}{m_2}, 0), 1), \min(\max(\frac{f_0^2 - \sum_{i=1}^2 m_i x_i^2}{m_2}, 0), 1)), \quad (24)$$

$$x_4 = \frac{f_0^2 - \sum_{i=1}^3 m_i x_i^2}{m_4}. \quad (25)$$

C. Uniformity analysis of pure state fidelity

We use a computer to generate 500 single-qubit pure states.

The fidelity between each of 500 pure states and the state $|0\rangle$ is $\sqrt{0.5}$. We also give a geometric representation of the Bloch

ball in FIG.3(a). It is obvious that the distribution of 500 states is uniform.

In addition, we verify the uniformity of four-qubit pure states fidelities. We generate 10,000 four-qubit pure states, in which the fidelity between each of these states and the state $|0000\rangle$ is 0.25. We select 20 states out of the 10,000 states, and the fidelity between each selected state and 9,999 other states can be calculated. We get 20 similar distributions, including the distribution of random state 6 and the distribution of the random state 20 in FIG.3(b). We conclude that the distribution of 10,000 states is uniform.

D. Uniformity analysis of mixed state fidelity

Here, we verify the uniformity of four-qubit mixed states datasets in FIG.3(c). A total of 1,220 states are generated, in which the fidelity between 1,220 states and the state $|0000\rangle$ is 0.25. We also select 20 states out of 1,220 states. The fidelity, between each selected state and the other 1,219 states, can be calculated. We get 20 similar distribution patterns, including the distribution of random state 6, random state 15 and the distribution of random state 20 in FIG.3(c). We found that the distribution of the 1,220 states is uniform.

E. Distribution of different purities of mixed states

The purity of a quantum state ρ is defined as $tr(\rho^2)$, where $tr(\rho^2) = 1$ means that this quantum state is pure and vice versa is a mixed state. FIG.4 shows the distribution of purity for 1,220 four-qubit mixed states, in which m_1 can control the purity of quantum states. In FIG.4(a-b) the fidelity f_0 between the prepared state and $|0000\rangle$ is 0.25, and the fidelity f_1 is 0.8 in FIG.4(c-d). The controller m_1 is equal to 1, 0.9, 0.6, 0.2 or 0.01. Moreover, m_1 can also be a uniform distribution $U(0, 1)$. The analysis here demonstrates how to control the purity of the prepared states.

Here, we discuss nine datasets in Table S2 for the four-qubit general state $|\varphi_4\rangle$, in which eight datasets belong to mixed states and the rest one to pure states. In eight mixed datasets, the purity distribution of m_1 is changed for seven datasets and the remaining one does not change the distribution of m_1 .

By comparing the distribution from Table S3, it can be seen that the distribution $m_1 = 1 - rand^3$ is better than others because this distribution is effective for mixed states and pure states. It is worth note that the states in this distribution $m_1 = 1 - rand^3$ are closer to pure states than those in other distributions. Here we only show the validation results of $k = 3, 4, 5$ of nine ANN models for nine datasets because from these results can draw the conclusion we give.

F. Universality of our method

We will prove the universality of our methods for preparing quantum states. To better demonstrate this inference, we show three dataset classes with three six-qubit general target pure states $|\varphi_6^1\rangle, |\varphi_6^2\rangle, |\varphi_6^3\rangle$, respectively. By analyzing the results from Table S4, we conclude that our method of preparing database is universal, corresponding to an arbitrary target pure state.

G. Poisson noise analysis

In an experiment, noise is inevitable. In our work, we assume that the noise follows the Poisson law. Using the *random* function in Matlab, we can obtain one value from the Poisson distribution with NP , in which P is the basis measurements, and NP is the ideal coincidence count.

We give a comparison of different number of samples for a four-qubit general state (See FIG.5). The noise model uses the number of samples of $N = 1,000, 4,000, 7,000, 10,000, 10,000$ and $1,000,000$. For comparison, we find that the noise model for the number of sample $N = 10,000$ is appropriate. Therefore, these datasets are generated with the number of samples $N = 10,000$ from two-qubit to seven-qubit states.

III. SELECTION OF PAULI COMBINATIONS

Let W_k ($k = 1, 2, \dots, 2^{2n}$) denotes all possible Pauli operators (n -fold tensor products of $(\sigma_x, \sigma_y$ and σ_z). Then $tr(\rho\sigma)$ can be rewritten in Ref.[1] as follows.

$$tr(\rho\sigma) = \sum_k \frac{1}{d} \chi_\rho(k) \chi_\sigma(k), \quad (26)$$

where the characteristic function is defined as $\chi_\rho(k) = tr(\rho W_k)$. For a target pure state ρ , we define the weight $Pr(k)$ corresponding to the Pauli operators W_k .

$$Pr(k) = [\chi_\rho(k)]^2, \quad (27)$$

If we want to know the fidelity between a target pure state and an arbitrary state, we need to get $\chi_\sigma(k)$ in Eq.(23) related to the weight $Pr(k) \neq 0$. Obviously, the general state requires more Pauli combinations than a special state. Here we have chosen the k Pauli operators with the largest absolute value of the expectation value of the desired quantum state.

Here we show the accuracy of the neural network for the Pauli operators with a large absolute value of expectation and for the Pauli operators with a small absolute value of expectation, respectively (See Table S5). Take the four-qubit cluster state and the general state as an example, the ANN model for the Pauli operator with a large absolute value of expectation can get more information than that for the Pauli operator with a small absolute value of expectation.

We then show the selected Pauli operators from two-qubit to seven-qubit states in Table S6.

IV. COMPARISON OF THE ACCURACY OF NEURAL NETWORK WITH TWO CLASSES OF INPUTS

In Table S7, we present the results of the artificial neural network trained with the probability of the measurement outcomes of the expectation and the artificial neural network trained with the expectation. The bases ANN represents that the inputs that are the probabilities of measurement. The expectation ANN represents that the inputs are the expectation values. It can be seen that the accuracy of the two kinds of neural network models is almost equivalent.

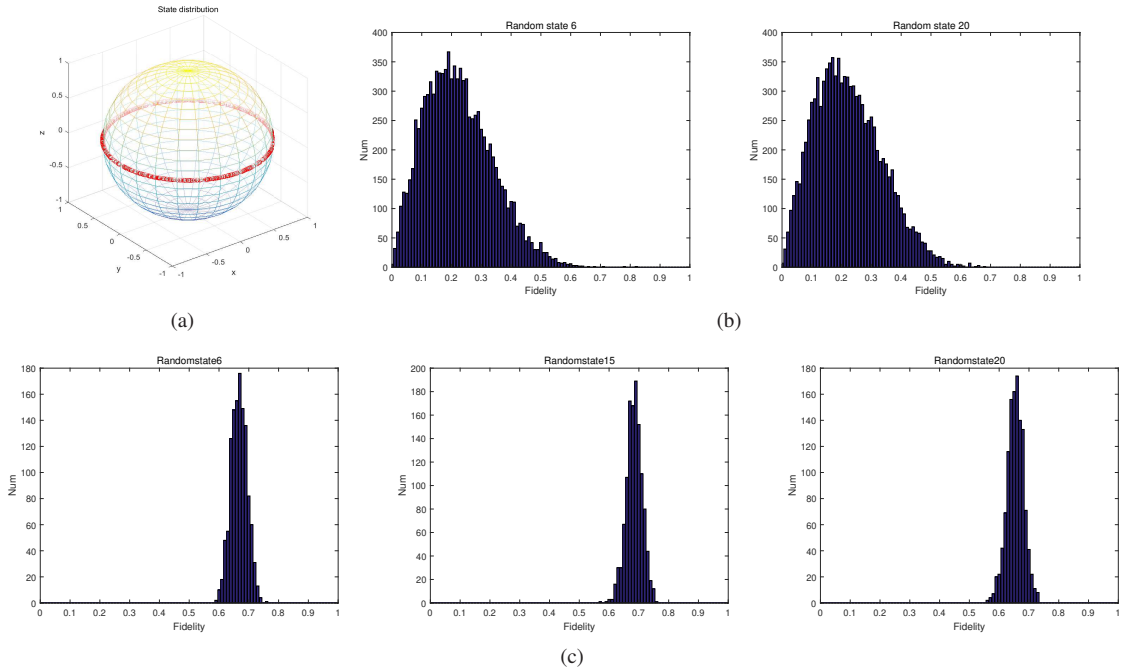


FIG. 6. (Color Online) (a) Distribution of 500 single-qubit states in the Bloch ball; (b) The distribution of 10,000 four-qubit pure states containing state 6 and state 20; (c) The distribution of 1,220 four-qubit mixed states including state 6, state 15 and state 20.

Table S2. Nine distributions of m_1

ANN models	datasets	m_1 distribution
A	1	$m_1 = 1 - \text{rand} * \text{rand}$
B	2	$m_1 = 1 - \sqrt{\text{rand}} * \text{rand}$
C	3	m_1 belongs to a uniform distribution $U(0, 1)$
D	4	m_1 belongs to a random standard normal distribution $N(0, 1)$
E	5	Pure states
F	6	$m_1 = 1 - \text{rand} * \text{rand} * \text{rand}$
G	7	$m_1 = 1 - \text{rand} * \text{rand} * \text{rand} * \text{rand}$
H	8	$m_1 = 1 - \text{rand}^3$
I	9	$m_1 = 1 - \text{rand} * \text{rand}^3$

V. PRECISION OF FIDELITY ESTIMATION

FIG.6 presents some important information about the neural network with different number of labels. In FIG.6(a-c), in the case of a fixed number of labels, the higher the number of Pauli operator measurement settings used, the higher the prediction accuracy is. Meanwhile, the higher the fidelity of the predicted quantum states is, the higher the accuracy is. In FIG.6(d), the more quantum state fidelity intervals are divided, the higher the accuracy is. However, the accuracy of the neural network model with 234 labels is not much higher than that of the neural network model with 122 labels. Moreover, the higher the number of labels are, the more resources and time are consumed, so the neural network with 122 labels is selected as the most appropriate. The fidelity interval of the quantum state is respectively divided into 66 labels, 122 labels and 234 labels for the specific interval in Ref.[4].

VI. ACCURACIES OF ANN MODELS FOR N-QUBIT STATES

In Table S8, we show all the accuracies of the ANN models from two-qubit to seven-qubit states with the precision $\pm 1\%$.

VII. APPLICATIONS OF OUR NEURAL NETWORKS

How can we use a trained neural network to determine whether the fidelity of an input quantum state is higher than 96%. The fidelity of this quantum state is first predicted using a neural network with $k = 2$. If the upper bound of the predicted fidelity range given does not exceed 96%, the neural network gives the prediction that determines that the fidelity of this state does not exceed 96%. If the lower bound of the predicted fidelity range is more than 96%, the neural network will give a prediction that the fidelity of this state is

Table S3. Accuracy of nine ANN models for nine datasets

datasets	1	2	3	4	5	6	7	8	9
\backslash model k	A								
3	79.78%	80.57%	81.11%	77.19%	72.60%	78.09%	76.41%	78.32%	77.12%
4	86.99%	87.33%	87.42%	83.37%	82.62%	86.34%	85.45%	86.10%	85.63%
5	89.82%	90.26%	89.94%	85.96%	87.26%	90.01%	89.48%	89.43%	89.59%
\backslash model k	B								
3	78.84%	80.24%	81.21%	77.61%	67.65%	76.47%	73.82%	77.04%	74.98%
4	86.34%	87.03%	87.36%	83.75%	78.13%	84.70%	82.97%	84.84%	83.57%
5	89.58%	90%	89.70%	86.49%	83.56%	88.89%	87.93%	88.65%	88.17%
\backslash model k	C								
3	77.53%	79.07%	80.29%	77.44%	66.83%	74.62%	71.98%	75.59%	75.59%
4	85.36%	86.32%	87.11%	83.61%	76.39%	83.14%	81.01%	83.69%	83.69%
5	88.67%	89.38%	89.72%	86.24%	81.36%	87.02%	85.34%	87.29%	87.29%
\backslash model k	D								
3	75.29%	77.62%	79.37%	76.67%	59.93%	70.81%	67.10%	72.51%	69.18%
4	82.65%	84.39%	85.60%	82.80%	69.73%	79.13%	76.01%	80.27%	77.61%
5	85.72%	86.91%	87.74%	85.26%	76.09%	83.25%	80.90%	83.89%	82.05%
\backslash model k	E								
3	22.93%	15.73%	11.10%	10.96%	85.05%	38.62%	54.07%	34.86%	46.63%
4	26.66%	18.21%	12.64%	12.63%	91.83%	44.57%	61.47%	39.29%	52.52%
5	27.60%	18.59%	12.49%	12.24%	95.07%	46.41%	64.04%	40.60%	54.55%
\backslash model k	F								
3	80.02%	80.13%	80.18%	76.15%	75.52%	79.66%	78.62%	79.19%	78.86%
4	87.47%	86.94%	86.49%	82.64%	85.10%	87.66%	87.48%	86.93%	87.10%
5	90.45%	90.24%	89.55%	85.58%	90.70%	91.27%	91.37%	90.46%	91.04%
\backslash model k	G								
3	79.13%	78.84%	78.65%	74.30%	78.77%	79.58%	79.67%	78.96%	78.39%
4	86.63%	85.97%	85.35%	81.16%	86.86%	87.63%	88.16%	86.78%	87.17%
5	90.43%	89.57%	88.58%	84.44%	91.87%	91.67%	92.25%	90.50%	90.92%
\backslash model k	H								
3	79.09%	79.51%	80.78%	76.93%	76.03%	78.37%	77.45%	78.65%	78%
4	87.26%	87.15%	86.80%	83.11%	84.64%	87.09%	86.27%	86.75%	86.58%
5	90.65%	90.32%	89.24%	85.77%	89.30%	90.94%	90.38%	90.28%	90.59%
\backslash model k	I								
3	79.73%	79.88%	79.15%	75.84%	76.82%	79.62%	79.18%	79.33%	78.65%
4	86.82%	86.36%	86.39%	82.18%	86.92%	87.30%	87.53%	86.79%	87.39%
5	90.08%	89.46%	88.81%	85.18%	91.23%	91%	91.46%	90.26%	91.08%

Table S4. Datasets comparison of three six-qubit general states

six-qubit (Hid-neu:1500-1500, precision with $\pm 1\%$)			
\backslash states k	$ \varphi_6^1\rangle$	$ \varphi_6^2\rangle$	$ \varphi_6^3\rangle$
2	78.61%	77.06%	78.75%
3	86.84%	86.32%	86.20%
4	91.39%	91.86%	91.51%
5	93.86%	95.20%	94.81%
6	96.18%	97.03%	96.67%
7	97.20%	98.01%	97.11%

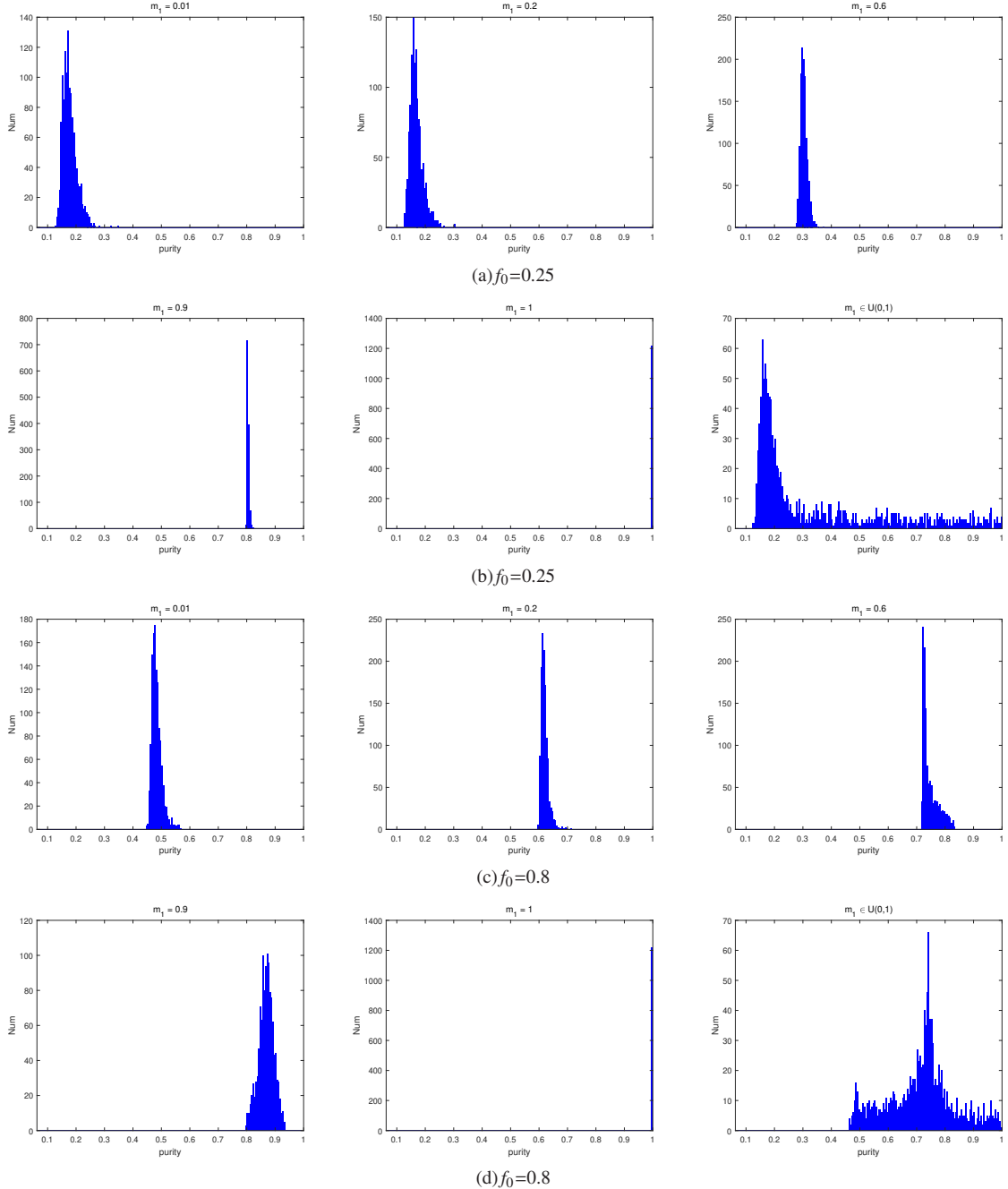


FIG. 7. (Color Online) Comparison of mixed-state distributions for different purity, where $m_1 = 1, 0.9, 0.6, 0.2, 0.01, U(0, 1)$. The specified quantum states fidelities are 0.25 and 0.8 respectively.

more than 96%. If the range of prediction fidelity is given including 96%, it is necessary to determine whether the prediction accuracy reaches $\pm 1\%$. If the prediction accuracy reaches $\pm 1\%$, the neural network determines that the fidelity of this state does not exceed 96%. If the prediction accuracy does

not reach $\pm 1\%$, the neural network cannot determine that the fidelity of this state does not exceed 96%. Therefore, we continue the prediction with the $k=3$ neural network and repeat the above test process. Finally, the neural network can determine whether the fidelity of this state exceeds 96%.

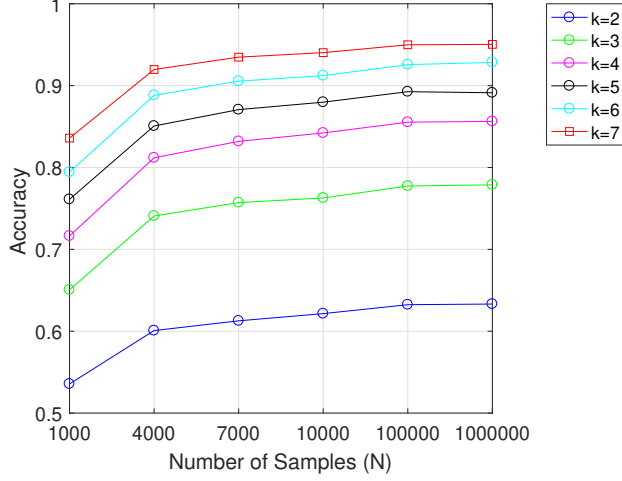


FIG. 8. (Color online) Comparison of the accuracy of neural network models with different number of samples. Taking a four-qubit general state as an example, when $k=2,3,4,5,6,7$, the neural network models with the number of samples 1000, 4000, 7000, 10000, 100000, 1000000 are generated respectively. The higher the number of Pauli operator measurement settings used, the higher the prediction accuracy is. The higher of the number of samples N is, the higher the accuracy is.

Table S5. Comparison of two types of weights

		four-qubit states (Precision $\pm 1\%$)					
		k	states	$ \varphi_4\rangle$ (largest weight, Hid-neu:5000)	$ \varphi_4\rangle$ (smallest weight, Hid-neu:5000)	Cluster (weight=1, Hid-neu:3000)	Cluster (weight=0, Hid-neu:3000)
2		62.15%		56.18%		90.91%	67.62%
3		76.28%		69.21%		96.65%	81.19%
4		84.22%		77.46%		98.73%	90.53%
5		87.98%		83.73%		99.60%	96.11%
6		91.22%		90.61%		99.86%	97.25%
7		94.03%		93.40%		99.98%	97.62%

- [2] M. Cramer, M. B. Plenio, S. T. Flammia, R. Somma, D. Gross, S. D. Bartlett, O. Landon-Cardinal, D. Poulin, Y. Liu, Efficient quantum state tomography, *Nature Communications* 1 (2010) 149.
- [3] F. Tacchino, C. Macchiavello, D. Gerace, D. Bajoni, An artificial neuron implemented on an actual quantum processor, *npj Quantum Information* 5 (2019) 26.
- [4] For 66 labels, the division of the fidelity is $[0 : 0.1 : 0.6, 0.61 : 0.02 : 0.8, 1 - \frac{0.98}{5} : \frac{0.02}{5} : 1]$. For 122 labels, the division of the

fidelity is $[0 : 0.05 : 0.6, 0.61 : 0.01 : 0.8, 1 - \frac{1.78}{9} : \frac{0.02}{9} : 1]$. For 234 labels, the division of fidelity is $[0 : 0.025 : 0.6, 0.605 : 0.005 : 0.8, 1 - \frac{3.38}{17} : \frac{0.02}{17} : 1]$. A selection of 66 labels, 122 labels and 234 labels is convenient for comparing results as the error bar can be set to $\pm 1\%$.

- [5] Here, we show the general states $|\varphi_2\rangle, |\varphi_3\rangle, |\varphi_4\rangle, |\varphi_5\rangle, |\varphi_6\rangle$ as follows.

Table S6. Pauli operators

two-qubit		three-qubit	
states	Pauli operators	states	Pauli operators
Bell	XX;YZ;ZY;YY;ZX;XZ;XY	GHZ	ZZZ;XXX;XYY;YXY;YYX;YYY;XXZ
W_2	XX;YZ;ZY;XZ;YY;ZX;ZZ	W	ZZZ;ZXX;ZYY;XZX;XXZ;YZY;YYZ
$ \varphi_2\rangle$	XY;ZX;YZ;XX;YY;ZZ;XZ	$ \varphi_3\rangle$	YYY;XXY;ZYY;XYZ;YXX;YXZ;YXY
four-qubit			
Cluster	ZZXX;ZZYY;XXXX;YYZZ;XYXY;XYYX;YXXX		
Dicke	XXXX;YYYY;ZZZZ;XXZZ;ZZYY;ZXXX;YYZZ		
GHZ	XXXX;YYYY;ZZZZ;XXYY;XYXY;YXXX;YYXX		
W	ZZZZ;ZZXX;ZZYY;XXZZ;YYZZ;XZXZ;YZYZ		
$ \varphi_4\rangle$	YXXX;XYZX;ZYYY;YZXX;XYZY;YXZZ;ZZYX		
five-qubit			
Cluster	XZZX;ZYXYZ;ZXZZX;YXXX;YYZZX;XZZYY;ZYXXX		
C-ring	XXXXX;ZYXYZ;ZZYXY;XYZZY;YXYZZ;YZZYX;XZZYX		
Dicke	ZZZZZ;XXXXZ;YYYYZ;ZZXXX;ZYYYY;YZZY;XXXZX		
GHZ	XXXXX;ZZZZZ;XYXXX;XYXYX;XYYXX;YXYYY;YYXYY		
W	ZZZZZ;XXZZZ;XZZXZ;YYZZZ;YZZYZ;ZXZXZ;ZYZZY		
$ \varphi_5\rangle$	YYXZX;XZZYZ;ZYYYY;XZYXX;XXZZY;YZXXZ;ZYXZY		
six-qubit			
C23	XZXYXY;XZXYXY;ZXYXYZ;ZYZYXZ;YXYXZX;XZXZYY;ZYZZXY		
Dicke	ZZZZZ;XXZZZ;ZZZZYY;ZZYYZZ;ZXZXZ;ZZXXZ;YYZZZZ		
GHZ	XXXXXX;YYYYYY;ZZZZZZ;XXXYYY;XYYYYYX;YXYYXY;YYYYXX		
W	ZZZZZ;XZXZZ;XZZZX;YYZZZ;YZZYZ;ZXZXZ;ZYZZY		
$ \varphi_6\rangle$	XXYXYX;ZXYZZZ;YYZYXZ;ZZXZXY;ZXYXYY;ZYZZZ;YZZYZY		
seven-qubit			
C34	XZXZYXY;ZYXYXZX;ZXYZZYZ;XZYYYYZ;YYYZZXY;YXXYXZX;XZXZZYY		

Table S7. Comparison of two classes of ANN inputs

A four-qubit general state (Hid-neu:5000, precision with $\pm 1\%$)		
k	Bases ANN	Expectation ANN
2	62.15%	61.47%
3	76.28%	77.06%
4	84.22%	84.84%
5	87.98%	88.47%
6	91.22%	91.86%
7	94.03%	94.22%

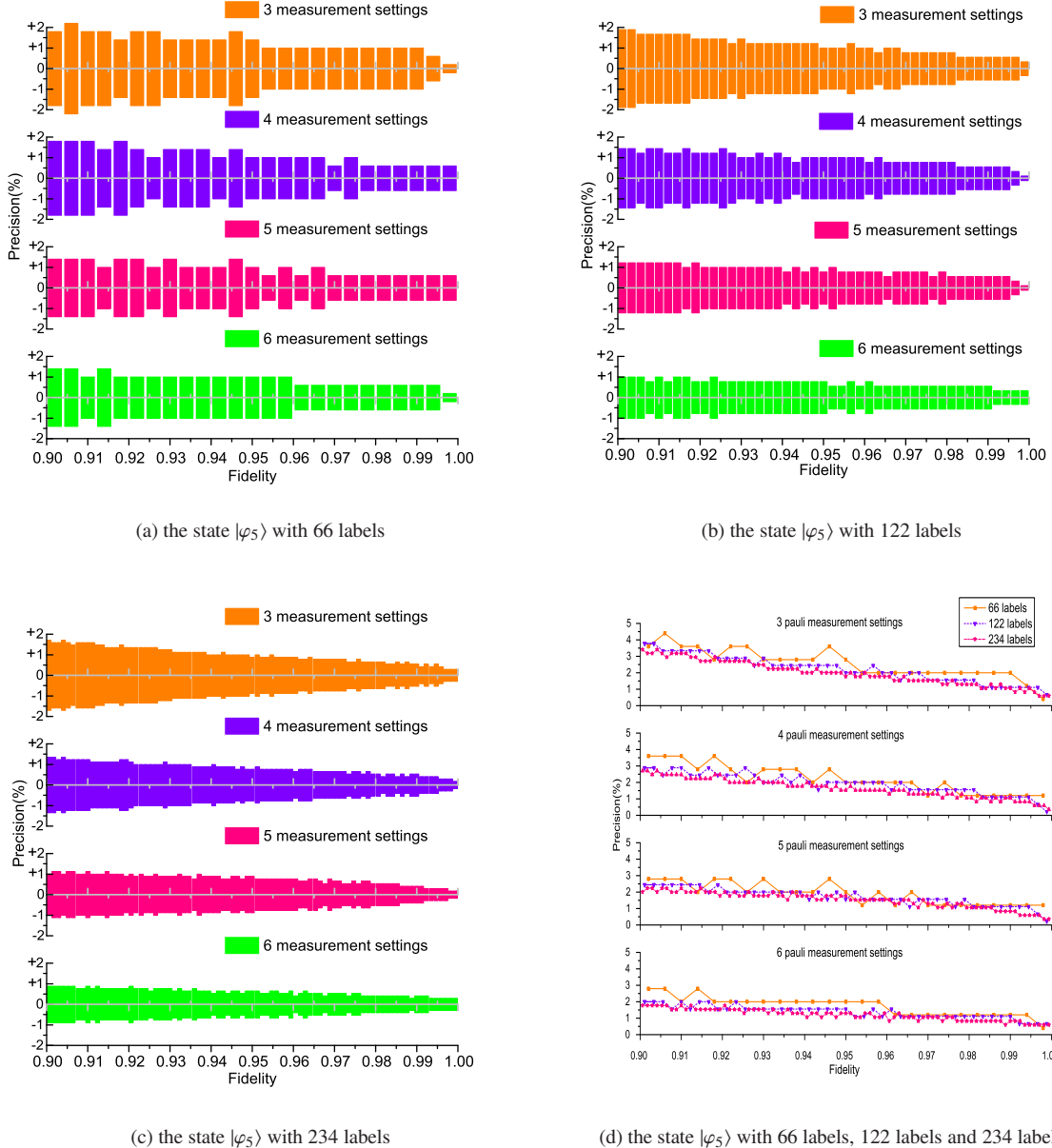


FIG. 9. (Color Online) A plot of the prediction accuracy of the neural network versus the quantum state fidelity when measurements are made using three, four, five, and six Pauli operator measurement settings. Here we choose a 5-qubit general state $|\varphi_5\rangle$ as the target state. The higher the number of Pauli operator measurement settings used, the higher the prediction accuracy is. The higher the fidelity of the predicted quantum states is, the higher the accuracy is. The more quantum state fidelity intervals are divided, the higher the accuracy is. However, the higher the number of labels are, the more resources and time are consumed, so the neural network model with 122 labels is selected as the most appropriate.

Table S8. Accuracies of ANN models

k	states	two-qubit (Hid-neu:2000)			three-qubit (Hid-neu:2000)		
		Bell	W_2	$ \varphi_2\rangle$	GHZ	W	$ \varphi_3\rangle$
2		58.48%	36.48%	36.06%	86.33%	73.68%	54.06%
3		71.68%	58.86%	62.19%	94.35%	79.95%	68.18%
4		87.03%	78.82%	76.16%	99.35%	90.60%	79.97%
5		88.08%	92.41%	80.23%	100%	97.51%	89.19%
6		88.75%	98.46%	87.09%	100%	99.71%	92.63%
7		91.32%	99.99%	93.43%	100%	99.99%	95.38%
k	states	four-qubit (Hid-neu:2000)					
		Cluster	GHZ	W	Dicke		$ \varphi_4\rangle$
2		92.95%	77.77%	86.40%	94.21%		61.52%
3		96.92%	97.77%	88.83%	97.40%		76.16%
4		97.90%	98.73%	93.32%	98.06%		83.67%
5		98.81%	99.47%	95.12%	98.74%		87.51%
6		99.13%	99.78%	96.64%	99.14%		91.26%
7		99.50%	99.98%	97.30%	99.55%		93.87%
k	states	five-qubit (Hid-neu:1500-1500)					
		Cluster	C-ring	Dicke	GHZ	W	$ \varphi_5\rangle$
2		84.41%	85.02%	89.94%	99.13%	96.16%	68.74%
3		96.04%	90.29%	96.56%	99.43%	97.19%	82.72%
4		97.91%	94.39%	97.59%	99.44%	97.38%	87.10%
5		98.47%	96.58%	98.60%	99.68%	97.88%	90.66%
6		99.40%	97.43%	99.21%	99.84%	98.19%	95.87%
7		99.51%	98.11%	99.63%	99.95%	97.62%	97.73%
k	states	six-qubit (Hid-neu:1500-1500)			seven-qubit (Hid-neu:1500-1500)		
		GHZ	C23	W	Dicke	$ \varphi_6\rangle$	C34
2		91.24%	98.23%	99.03%	96.12%	78.61%	99.81%
3		99.89%	98.59%	99.17%	97.25%	86.84%	99.82%
4		99.95%	98.77%	99.57%	98%	91.39%	99.94%
5		99.94%	99.76%	99.67%	98.30%	93.86%	99.96%
6		99.95%	99.84%	99.66%	98.96%	96.18%	99.97%
7		99.98%	99.92%	99.75%	99.07%	97.20%	99.99%

$$\begin{aligned}
|\varphi_2\rangle &= [0.0405; -0.4803 - 0.3933i; -0.0253 + 0.6459i; -0.3755 + 0.2327i] \\
|\varphi_3\rangle &= [0.1187; 0.0345 + 0.0223i - 0.1228 + 0.3747i; 0.5924 - 0.2336i; -0.0357 + 0.4961i; \\
&\quad 0.1944 + 0.2406i; -0.0454 - 0.0279i; 0.0690 + 0.2696i], \\
|\varphi_4\rangle &= [0.1392; 0.2107 + 0.0414i; -0.2524 - 0.2647i; 0.2062 - 0.1354i; 0.1718 - 0.0116i; 0.1064 + 0.1494i; \\
&\quad 0.0789 - 0.0398i; -0.2188 + 0.3383i; -0.0520 - 0.1559i; -0.1901 + 0.1452i; -0.0245 - 0.4181i; \\
&\quad 0.1251 + 0.3846i; -0.1304 + 0.0025i; 0.0941 + 0.0955i; -0.0577 - 0.1087i; -0.1465 + 0.1079i], \\
|\varphi_5\rangle &= [0.1592; 0.0474 - 0.1834i; -0.0431 - 0.1664i; -0.3363 - 0.0787i; -0.0380 - 0.1645i; 0.0378 - 0.0606i; \\
&\quad -0.0846 + 0.2026i; 0.1586 + 0.2416i; 0.1116 - 0.0157i; 0.1064 + 0.0906i; 0.0608 - 0.1556i; 0.0302 - 0.0418i; \\
&\quad -0.0254 - 0.0624i; -0.0319 - 0.2507i; 0.0381 - 0.1123i; -0.1093 - 0.1652i; -0.0873 - 0.1461i; 0.1807 - 0.1654i; \\
&\quad 0.2658 + 0.0427i; -0.2010 - 0.0322i; 0.0356 - 0.0686i; 0.1222 + 0.0009i; 0.0944 + 0.1331i; 0.0080 + 0.0417i; \\
&\quad -0.0748 - 0.0483i; 0.0762 + 0.0756i; 0.1541 - 0.0227i; -0.1414 + 0.1879i; -0.1427 + 0.0462i; -0.1530 - 0.0816i; \\
&\quad 0.0003 - 0.1342i; -0.1308 - 0.0317i], \\
|\varphi_6\rangle &= [0.1258; -0.1289 - 0.0911i; -0.0347 + 0.0199i; -0.0120 - 0.0352i; -0.0198 + 0.1522i; 0.0906 + 0.0063i; \\
&\quad 0.0262 + 0.1211i; -0.0544 - 0.0378i; -0.0938 - 0.0502i; 0.1184 - 0.0093i; 0.0254 - 0.0371i; 0.0822 + 0.0523i; \\
&\quad 0.0656 - 0.1028i; -0.0115 - 0.0604i; 0.1542 + 0.1956i; 0.0795 - 0.1196i; -0.0635 - 0.1297i; -0.0263 + 0.0456i; \\
&\quad -0.0209 + 0.1140i; -0.0203 + 0.1012i; 0.0056 - 0.1283i; 0.0080 - 0.1463i; -0.0337 + 0.0195i; 0.1088 + 0.0836i; \\
&\quad -0.0252 - 0.1061i; 0.0056 + 0.0136i; -0.0605 - 0.1446i; -0.0780 - 0.0079i; 0.0728 - 0.0672i; 0.0632 - 0.0174i; \\
&\quad 0.0429 + 0.1532i; 0.1260 + 0.1066i; -0.0437 - 0.2037i; 0.0194 - 0.1971i; 0.0806 - 0.1285i; 0.0289 + 0.0105i; \\
&\quad 0.1379 - 0.0677i; -0.0626 + 0.0409i; -0.0276 + 0.0982i; -0.1363 - 0.1521i; 0.0483 + 0.0272i; -0.1545 - 0.0268i; \\
&\quad -0.0652 - 0.0775i; -0.1179 + 0.1717i; 0.0720 - 0.0315i; -0.0931 + 0.1785i; 0.0109 + 0.1410i; 0.0057 + 0.0447i; \\
&\quad -0.0246 + 0.0696i; -0.0725 - 0.0747i; 0.0096 - 0.0414i; 0.0934 - 0.0460i; -0.1239 - 0.1170i; -0.0751 + 0.1246i; \\
&\quad -0.1074 + 0.0287i; 0.1096 + 0.1297i; -0.0941 - 0.0287i; -0.0138 - 0.0076i; -0.0870 + 0.1829i; -0.0824 + 0.0722i; \\
&\quad 0.1162 + 0.0492i; 0.0326 + 0.0584i; -0.0073 + 0.0186i; -0.0626 - 0.0719i]
\end{aligned} \tag{28}$$